

Revealing Cracking and Breakage Behaviours of Gibbsite Particles

Jinxuan Zhang¹, Lei Ge^{1,3}, Zhi-Gang Chen²*, Zhonghua Zhu¹*

1 School of Chemical Engineering, University of Queensland, Brisbane, Queensland 4072,
Australia.

2 School of Materials Engineering, University of Queensland, Brisbane, Queensland 4072,
Australia.

3 Centre for Future Materials, University of Southern Queensland, Springfield, Queensland
4300, Australia

Corresponding Author

*Lei Ge. E-mail: lei.ge@usq.edu.au

*Zhi-Gang Chen. E-mail: zhigang.chen@uq.edu.au

ABSTRACT

Mitigating gibbsite particle cracking and breakage during industrial alumina production can increase the quality of smelter grade alumina product by reducing the ultrafine particle content. Therefore, it is essential to investigate the particle cracking during static calcination and the breakage of calcined gibbsite particles under external force. In this work, we investigated the impact of the calcination ramping rate and the crystallite size on gibbsite particle cracking during static calcination. A slow ramping rate and a large pristine crystallite size tend to increase particle cracking. Apart from the study of particle cracking behaviour, we also investigated the breakage of calcined gibbsite particle under external force. Cracks on the particle surface can initiate breakage within the crystallite and along the grain boundary under external force. The breakage within crystallite occurs as the cleavage of the crystallite, while the breakage along the grain boundary leads to the shedding of a whole crystallite. We further explored the factors influencing the strength of calcined gibbsite particles. With increasing calcination temperature, the strength of particle increases when gibbsite converts to boehmite, and then decreases when boehmite converts into amorphous alumina. Particles containing smaller crystallites and calcined with fast ramping rates exhibit higher resistance to breakage.

KEYWORDS: Gibbsite particle, calcination, cracking, breakage.

1 Introduction

Smelter grade alumina (SGA) is the major raw material applied in aluminium production, and it is primarily produced by alumina refining via the Bayer process¹⁻³. In Bayer process, heated alkali is applied to dissolve the aluminium hydroxide and oxide contained in bauxite, thus preparing the pregnant sodium aluminate solvent^{4,5}. Next, ultrafine gibbsite particles are added into the sodium aluminate solvent as the crystallization seed after removal of the solid residue. The dissolved aluminium precipitates as gibbsite crystallites. The crystallites then collide and form mosaic and radial gibbsite particles^{6,7}. Mosaic particles consist of crystallites of smaller size and it is produced by feeding narrowly size-distributed ultrafine gibbsite particles uniformly into pregnant sodium aluminate solvent. On the other hand, radial gibbsite mainly consists of relatively larger crystallites and it is produced via a feeding of broad-size distributed fine gibbsite particle in large quantity^{8,9}. Then SGA can be prepared by calcining the gibbsite particles. In calcination aluminium hydroxide converts to aluminium oxide. The produced SGA can be further applied as a feedstock in the aluminium production by electrochemical reduction of the SGA dissolved in the electrolyte bath^{10,11}.

During industrial production, ultrafine particles can be generated due to gibbsite particle breakage during calcination. A series of detrimental effects can be caused by ultrafine particles contained in the downstream aluminium production. First, increased ultrafine particle content can lead to insufficient or excessive SGA feeding into the reduction cell by making the feeding flow inconsistent. Insufficient SGA feeding can cause electrolyte bath reduction thus increasing the perfluorocarbons emission, while excessively fed SGA can sludge on the cathode and worsen the process control¹². Apart from inconsistent feeding, previous research emphasized that ultrafine particles tend to be relatively higher in impurity content. The impurity in SGA results in dissolving problems and increased environment-damaging emission^{13,14}. Moreover, other side effects including material waste, dust pollution and hygiene

problems are also attributed to the ultrafine particles in SGA product. Therefore, it is essential to understand and inhibit the gibbsite particle breakage during calcination.

Previous research pointed out that cracks can be found on particle surfaces after static calcination while the particle size distribution does not change significantly¹⁵. Cracks can be found on the crystallite and grain boundary of gibbsite particle. The cracks on gibbsite crystallite are initiated as the slit pores inside the crystallite bulk during calcination, then pores grow towards the surface and form open cracks and internal cracks¹⁶. On the other hand, the cracks on gibbsite grain boundary are initiated on the particle surface and then grow into the particle bulk with further calcination¹⁷. The cracks generated during calcination are considered to cause particle embrittlement, and it is the external force applied to the particles that directly initiate particle breakage^{13, 18-20}. In this work, we first aimed to analyse the impact of the calcination method and particle morphology on gibbsite particles' cracking behaviour during static calcination. Then we observed the debris of calcined gibbsite particles broken under external force and proposed a breakage mechanism. Thirdly, we investigated the impact of the calcination method and particle structure on the calcined gibbsite particle strength.

2 Experiment

2.1 Sample preparation

The mosaic and radial gibbsite particles are from South 32 Worsley Alumina Pty Ltd, their SEM images and the crystallite c-axis length distribution of mosaic and radial gibbsite are given in **Figure S1**. In order to prepare gibbsite particles calcined at different temperatures, mosaic and radial gibbsite particles were calcined at 400 °C and 800 °C for 5 hours respectively. The particles were calcined with a ramping rate of 10 °C • min⁻¹ in static air.

In order to prepare gibbsite particles calcined at different ramping rates, mosaic and radial gibbsite particles were calcined in static air with a ramping rate of 10 °C • min⁻¹ and a burst

rate respectively. The calcination temperature was 400 °C and the calcination duration was 5 hours. As for particles prepared at 10 °C • min⁻¹, the gibbsite particle before calcination was inserted into the oven and heated from room temperature. As for the particles prepared by burst calcination, the oven was previously heated to 400 ° C and then the gibbsite particles were quickly inserted into the calciner.

2.2 Characterisation

The calcined gibbsite particles were previously dried at 120 °C overnight then measured by an Autopore IV mercury porosimeter with a pressure up to 60000 psi. Based on the SEM observation, the total crack volume of each sample was considered as the cumulative intrusion volume within the diameter range from 5 nm to 300 nm.

The cracks on calcined gibbsite particles were inspected by a JEOL 7001 SEM apparatus. The crack width was measured and counted using Image J 1.46 based on over 100 SEM images with 1 or 2 cracks in each, and the crack width distribution was calculated.

A single particle impact (SPI) apparatus was utilized to break the calcined gibbsite particles by simulating the external force applied to the particles during industrial production. The particle size distribution of gibbsite particles was measured before and after breakage with an AccuSizer and the maximum cumulative volume difference (MCVD) of different particles was calculated. MCVD is the maximum difference between the cumulative volumes before and after breakage, and its increase indicates an increment in the formation of fragile particles. A JEOL 7001 SEM was applied to inspect the debris of particles after breakage by SPI and the mechanism of calcined gibbsite particle breakage under external force was proposed based on the SEM observation.

3 Results and discussion

3.1 Investigation of gibbsite particle cracking during static calcination

3.1.1 The impact of calcination ramping rate on the cracking of gibbsite particles

By comparing the total crack volume, average crack width and crack width distribution of gibbsite particles calcined with $10\text{ }^{\circ}\text{C} \cdot \text{min}^{-1}$ and burst ramping rate, it can be found that the ramping rate adopted in the static calcination can influence gibbsite particle cracking.

As found in the mercury porosimetry results, the total crack volume of the mosaic particles calcined at $400\text{ }^{\circ}\text{C}$ with a ramping rate of $10\text{ }^{\circ}\text{C} \cdot \text{min}^{-1}$ ($0.034 \pm 0.002\text{ mL/g}$) significantly exceeds the total crack volume of the mosaic particles calcined with burst calcination ($0.026 \pm 0.001\text{ mL/g}$) by 31%. Similarly, in radial samples, the total crack volume in particles calcined at $10\text{ }^{\circ}\text{C} \cdot \text{min}^{-1}$ ($0.040 \pm 0.005\text{ mL/g}$) exceeds the total crack volume in the radial particles prepared by burst calcination ($0.028 \pm 0.002\text{ mL/g}$) by 30%. By comparing the total crack volume of gibbsite calcined with different ramping rate, it can be found that gibbsite particles tend to generate more crack when prepared at decreased ramping rate.

Besides, the cracks generated on gibbsite particles calcined with decreased ramping rate also tend to be larger in width. **Figure 1a to d** presents the SEM images of cracks generated in mosaic gibbsite particles calcined at $400\text{ }^{\circ}\text{C}$ with $10\text{ }^{\circ}\text{C} \cdot \text{min}^{-1}$ and burst rate. As can be seen in the SEM images, the crack width increases on crystallites and grain boundaries when burst ramping rate is adopted.

The crack width distributions of mosaic particles calcined at $400\text{ }^{\circ}\text{C}$ with a ramping rate of $10\text{ }^{\circ}\text{C} \cdot \text{min}^{-1}$ and burst rate were also measured and counted. The crack width distributions are presented in **Figures 1e and f**. In mosaic gibbsite particles, with calcination ramping rate decreased from burst rate to $10\text{ }^{\circ}\text{C} \cdot \text{min}^{-1}$, the peaks of crack width in single crystallite shift from around 40 nm to around 90 nm and the average width of cracks on crystallite increases by 48%, from 55 nm to 82 nm. The peaks of crack width in grain boundary shifts from the around 70 nm to around 120 nm and the average width of cracks on particle grain boundary

increases by 30%, from 81 nm to 116 nm. Similarly in radial gibbsite particles, with decreased calcination ramping rate from burst rate to $10\text{ }^{\circ}\text{C} \cdot \text{min}^{-1}$, the peaks of crack width in single crystallite and grain boundary shift to a higher value as presented in **Figure S2**. By comparing the crack width distribution of gibbsite calcined with a different ramping rate, it can be found that slow ramping rates can lead to wider crack generation on gibbsite particles during calcination. In summary, the mercury porosimetry measurement and the SEM statistical analysis results suggest that the low heating rate in calcination tends to increase the crack width and the total crack volume.

The mechanism of particle cracking during calcination can be used to explain the inhibition of crack generation in gibbsite crystallites by increasing calcination ramping rate. As mentioned in our previous works¹⁶, the generation of cracks in crystallite is initiated by the appearance of pores inside the bulk of crystallites, which appears at the interface between phase transformed and untransformed parts inside the bulk of crystallites. With further calcination, the stress generated due to crystallite shrinkage accumulates on the pores, and such pores can grow and generate cracks. Some of these cracks grow through the surface and generate open cracks while the majority of cracks are still hidden in the crystallite bulk.

When a higher calcination ramping rate is adopted in calcination, the phase transformation in the crystallite bulk is less uniform. Consequently, more pores appear inside the crystallite bulk. As shown in **Figure 2a**, with more pores dispersing the stress generated due to the crystallite shrinkage during calcination, less stress is likely to accumulate on every single pore and it would be more difficult for these pores to grow through the surface and become open cracks. As a result, the cracks that appear on the crystallite surface during calcination with an increased ramping rate tend to be small in width since they majorly grow from pores closer to the crystallite surface. Besides, gibbsite particles also tend to create cracks smaller in width on

their grain boundaries when calcined with increased ramping rate since the stress is dispersed by pores in crystallite bulk and less stress can accumulate on the grain boundary.

On the other hand, when calcined with a decreased calcination ramping rate, the phase conversion is more uniform and fewer pores are likely to appear in the crystallite bulk. As depicted in **Figure 2b**, the stress generated due to crystallite shrinkage during calcination is not well dispersed, and higher stress can be exerted on every single pore. Both pores closer to the crystallite surface and deeper in bulk can grow through the surface. As a result, wider and more cracks appear when particles are calcined with a slower ramping rate. Moreover, with less stress dispersed by pores in the crystallite bulk, more stress is likely to accumulate on grain boundary. Consequently, gibbsite particles tend to create cracks larger in width on their grain boundaries when calcined with decreased ramping rate.

3.1.2 The impact of crystallite size on gibbsite particle cracking

By comparing the total volume and width distribution of cracks on gibbsite particles calcined with the same calcination ramping rate, it can be concluded that the particle size of the crystallites also influences the particle cracking during static calcination. As found in the mercury porosimetry results, the total crack volume of radial gibbsite calcined at 400 °C with 10 °C •min⁻¹ (0.040±0.005 mL/g) exceeds the total crack volume of mosaic particles calcined with the same method (0.034±0.002 mL/g) by 18%. These data indicate that radial gibbsite particles tend to generate more cracks than mosaic gibbsite particles.

The SEM images of cracks generated on the mosaic and radial gibbsite particle surface during calcination at 400 °C with 10 °C•min⁻¹ are presented in **Figure 3a to d**. As displayed in the SEM images, radial particles generated larger cracks on the crystallite and grain boundaries when prepared with the same calcination method.

The width distribution of cracks generated on mosaic and radial particles are presented in **Figure 3e** and **f**. As presented in **Figure 3e**, the peak of crack width on single crystallite of mosaic and radial particles lies in the 50-180 nm and 60-300 nm ranges respectively. The average crack width on the crystallite of the radial particle (162 nm) is twice the average width of cracks on the crystallite of the mosaic (81 nm). Similarly, in **Figure 3f**, the peak width of cracks on mosaic and radial particles' grain boundary lies in the 40-220 nm and 80-320 nm ranges, respectively. The average width of cracks on the grain boundary of the radial particle (224 nm) exceeds the mosaic (115 nm) by 94%. The result in **Figure 3** indicates that radial particles tend to generate wider cracks than mosaic particles. The mercury intrusion results (Figure S3) also indicate the increment of total crack volume.

The tendency for radial gibbsite particles to generate wider cracks is attributed to the larger crystallites consisting of them. As previously mentioned, the crack generation is mainly due to crystallite shrinkage during calcination¹³. The crystallite axis is longer in radial gibbsite since radial gibbsite particles mainly consist of larger crystallites¹⁷. The cracks tend to grow wider with higher levels of stress accumulating during calcination. Moreover, the crack generation on the grain boundary is attributed to the shrinkage of the neighbour crystallites. As mentioned previously, the crystallite axis of gibbsite crystallites is longer in radial particles. The grain boundary is more likely to crack with higher stress accumulation.

3.2 Breakage of calcined gibbsite particles under external force

3.2.1 The breakage mechanism of calcined gibbsite particle under external force

The calcined gibbsite particle debris after breakage by single-particle impact apparatus (SPI) apparatus is observed by SEM. Based on the SEM observation, a breakage mechanism of calcined gibbsite particle under external force is proposed.

The scheme and picture of the SPI apparatus are shown in **Figure S4**. In the SPI apparatus, the particles are fed into the acceleration tube with a sample feeder. The particles are then accelerated by the vacuum and hit the target plate to break them.

Gibbsite particle breakage was found to occur within the crystallite and among the crystallites. The SEM image in **Figure 4a** displays the debris of calcined gibbsite particles generated by the breakage taking place within crystallite. As presented in the image, a relatively smooth plate is found at the edge of the section (indicated by the yellow arrow), specifying that the cracks on the crystallites can initiate the breakage within them. Meanwhile, the inner part of the section is coarse (indicated by the blue arrow), indicating that the particle breakage in crystallite is due to the crystallite cleavage. The SEM image in **Figure 4b** presents debris of calcined mosaic and radial gibbsite generated by breakage along the grain boundary. As found in the image, the section edge is relatively regular in shape (indicated by the red arrow). Moreover, compared with the debris generated due to the crystallite breakage, the section is relatively smooth (indicated by the blue arrow), specifying that the particle breakage on grain boundary is a whole crystallite coming off.

Based on the above mentioned results, a mechanism of calcined gibbsite breakage is proposed and given in **Figure 4c** and **d**. The gibbsite particle breakage on the crystallite is initiated by the cracks on the surface, since the cracks are reported to be fragile parts where the stress caused by external force is likely to accumulate^{18, 19}. The breakage then extends into the crystallite and causes the cleavage of crystallites. Therefore, the section within crystallite tends to be coarse. Different from the breakage which happens in the crystallite, the breakage on the grain boundary is more likely to extend along the grain boundary since grain boundaries are weaker parts in the particles²¹⁻²³. Hence, the breakage along the grain boundary is considered as a process in which a whole crystallite comes off by grain boundary rupture due to the external force, leaving a smooth section.

3.2.2 The impact of calcination temperature, crystallite size and calcination ramping rate on the strength of calcined gibbsite particle

In order to determine the impact of calcination temperature, calcination ramping rate and crystallite size on the strength of calcined gibbsite particles, the particle size distribution before and after breakage is measured and the maximum cumulative volume difference (MCVD) of mosaic and radial gibbsite prepared with different calcination method is calculated.

Figure 5a and **b** show the MCVD calculation results. As presented in **Figure 5a**, the cumulative volume difference (CVD) at different particle diameters is collected and presented in **Figure 5b**. The peak of the CVD curve is noted as MCVD. High MCVD value indicates fragile particles.

The MCVD of mosaic and radial gibbsite calcined at different temperatures with $10\text{ }^{\circ}\text{C} \cdot \text{min}^{-1}$ ramping rate is presented in **Figure 5c**, showing that the strength conversion of gibbsite calcined at increasing calcination temperature can be divided into two periods. The first period is from room temperature to $400\text{ }^{\circ}\text{C}$. In this period, the MCVD decreases by 68% (from around 19 to around 6) in mosaic particles and 50% (from around 20 to around 10) in radial particles. This indicates the particles are becoming significantly tougher. The second period is from $400\text{ }^{\circ}\text{C}$ to $800\text{ }^{\circ}\text{C}$. In this period, the MCVD of radial particles climbs back by 50%, from around 10 to around 15, and the MCVD of mosaic particles recovers from around 6 to around 12. The observed increment of MCVD indicates that the particles are becoming fragile when the temperature increases from $400\text{ }^{\circ}\text{C}$ to $800\text{ }^{\circ}\text{C}$.

It can also be found in **Figure 5c** that radial gibbsite particles before calcination have a slightly higher MCVD than mosaic gibbsite particles. When gibbsite converts to boehmite, the MCVD of mosaic gibbsite drops more sharply than radial, and the MCVD of mosaic particle is 40% lower than radial gibbsite. The MCVD of mosaic gibbsite is also 20% lower than radial gibbsite

when boehmite converts to amorphous alumina. By summarizing the results given above, it can be concluded that calcined mosaic gibbsite tends to be tougher than radial gibbsite, which corresponds to previous literatures²⁴⁻²⁷.

Apart from the calcination temperature and the size of crystallites consisting of particles, the ramping rate is also considered to influence the strength of the calcined gibbsite particles. The MCVD of mosaic gibbsite calcined at a different temperature with a burst rate and a ramping rate of $10\text{ }^{\circ}\text{C}\cdot\text{min}^{-1}$ are presented in **Figure 5d**. As presented, the MCVD of the mosaic particles calcined by burst calcination is around 4, which is only half of the MCVD of the particles calcined at $10\text{ }^{\circ}\text{C}\cdot\text{min}^{-1}$. With a further calcination temperature increase to $800\text{ }^{\circ}\text{C}$, the MCVD curve of mosaic gibbsite by burst calcination bounces back slightly to around 5, while the MCVD of the particles calcined at $10\text{ }^{\circ}\text{C}\cdot\text{min}^{-1}$ reaches to around 12. These phenomena indicate that the particles prepared by burst calcination are tougher than those calcined at a calcination ramping rate of $10\text{ }^{\circ}\text{C}\cdot\text{min}^{-1}$. A similar tendency is found in radial particles, as presented in **Figure S5**. The MCVD of a radial particle calcined by burst calcination is only 60% of the MCVD of a radial particle calcined with a ramping rate of $10\text{ }^{\circ}\text{C}\cdot\text{min}^{-1}$ at $400\text{ }^{\circ}\text{C}$ and 50% at $800\text{ }^{\circ}\text{C}$, indicating that the radial particles calcined with burst calcination tend to be tougher than those calcined with $10\text{ }^{\circ}\text{C}\cdot\text{min}^{-1}$. Based on the results given in **Figure 5d** and **S5**, it can be summarized that gibbsite particles calcined at higher calcination ramping rate tend to be tougher than those calcined at lower calcination ramping rate.

The strength conversion tendency at increasing calcination temperature is a combined result of material conversion and crack growth. As found in **Figure 5c**, the particle strength increases when the calcination temperature increases from room temperature to $400\text{ }^{\circ}\text{C}$. In this period, the major component of particle converts to boehmite at $260\text{ }^{\circ}\text{C}$ ^{16, 17}. Boehmite has higher strength than gibbsite^{28, 29}. Meanwhile, the particle embrittlement effect caused by crack is not significant since the cracks are relatively low in width and volume. The component conversion

to tougher material overcomes the particle embrittlement caused by the increase in crack width and volume, and particle strength increases as a result. Then the particle strength decreases when the temperature increases from room 400 °C to 800 °C. In this period, boehmite converts to amorphous alumina at 470 °C^{16, 17}. Though amorphous alumina is of higher strength than boehmite, the particles still experience significant embrittlement due to the crack growth at increased calcination temperature^{16, 17}. The particle embrittlement caused by the crack growth overweighs the component conversion to stronger material and causes a decrease in particle strength.

The calcination ramping rate and the size of crystallites consisting of gibbsite particles can influence the calcined gibbsite particle strength by influencing the total crack volume and crack width distribution on the calcined particles since cracks can be the defect point where breakage is likely to be initiated^{18, 19}. The particle embrittlement caused by cracks is more significant in gibbsite particles consisting of larger crystallites and calcined with lower ramping rates since these samples tend to generate cracks with increased total volume and crack width distribution. Consequently, the gibbsite particles consisting of larger crystallites and calcined with lower ramping rates tend to be more fragile under external force.

4 Conclusions

In this study, the cracking of gibbsite particles during various static calcination conditions and the breakage of calcined gibbsite particles under external force were investigated. With the calcination ramping rate decreasing from burst rate to 10 °C • min⁻¹, the total crack volume and the average width of crack in calcined gibbsite samples increases by over 30%. Gibbsite particle's crack generation can be inhibited by increased ramping rate is attributed to the decreased pore generation in the crystallite bulk when calcined with higher ramping rate. The total crack volume of calcined radial gibbsite particles exceeds mosaic particles by 18%, and the average widths of cracks from both crystallite and grain boundary in the radial particles

were significantly larger than those from the mosaic gibbsite particles. This tendency is attributed to the increased stress accumulation in the radial gibbsite with longer crystallite axis. Cracks on the calcined gibbsite particle surface can initiate the particle breakage under external force. The particle breakage was found to occur within crystallite and along the grain boundary. The crystallite breakage is found to be a crystallite cleavage process, while the breakage along the grain boundary is due to the grain boundary rupture. The particle strength conversion tendency at increasing calcination temperature is considered as the combined result of particle embrittlement caused by the crack growth and the material conversion to a tougher component. Mosaic particles tend to have higher strength than radial particles when calcined with the same ramping rate. The faster calcination ramping rate can benefit the maintenance of the particle strength and reduce the breakage. The findings from this study can provide a fundamental understanding of fines formation during the SGA production, thus providing potential guidance to mitigate fine particle content in SGA production.

ACKNOWLEDGEMENT

The authors acknowledge the support from the Australian Research Council Linkage project LP140100992.

REFERENCES

1. Lavoie, P.; Taylor, M.; Metson, J., A Review of Alumina Feeding and Dissolution Factors in Aluminum Reduction Cells. *Metallurgical and Materials Transactions B* **2016**, *47*, 2690–2696.
2. Sadighi, S.; Mohaddecy, R.; Ameri, Y., Artificial Neural Network Modeling and Optimization of Hall-Heroult Process for Aluminum Production. *International Journal of Technology* **2015**, *3* (6), 480-491.
3. Coursol, P.; Dufour, G.; Coté, J.; Chartrand, P.; Mackey, P., Application of Thermodynamic Models for Better Understanding and Optimizing the Hall–Heroult Process. *The Journal of The Minerals, Metals & Materials Society* **2012**, *64* (11), 1326-1333.

4. Authier-Martin, M.; Forté, G.; Ostap, S.; See, J., The Mineralogy of Bauxite for Producing Smelter-Grade Alumina. *The Journal of The Minerals, Metals & Materials Society* **2001**, (36-40).
5. Ruan, S.; Shi, L.; Li, J.; Gerson, A., Mechanism and kinetics of gibbsite-seeded sodium aluminosilicate crystallisation from synthetic spent Bayer liquor. *Hydrometallurgy* **2016**, *163*, 1-8.
6. Livk, I.; Ilievski, D., A macroscopic agglomeration kernel model for gibbsite precipitation in turbulent and laminar flows. *Chemical Engineering Science* **2007**, *62* (14), 3787-3797.
7. Sonthalia, R.; Behara, P.; Kumaresan, T.; Thakre, S., Review on alumina trihydrate precipitation mechanisms and effect of Bayer impurities on hydrate particle growth rate. *International Journal of Mineral Processing* **2013**, *125*, 137-148.
8. Belaroui, K.; Pons, M.; Vivier, H.; Meijer, M., Wet grinding of gibbsite in a bead-mill. *Powder Technology* **1999**, *105*, 396-405.
9. Belaroui, K.; Pons, M.; Vivier, H., Morphological characterisation of gibbsite and alumina. *Powder Technology* **2002**, *127*, 246-256.
10. Ž. Lubyová, P. F., J. Gabčová, Solubility and Rate of Dissolution of Alumina in Cryolite-Based AIF₃ of LiF, CaF₂. *Chemical Papers* **1993**, *47* (4), 218-220.
11. Yang, Y.; Gao, B.; Wang, Z.; Shi, Z.; Hu, X., Effect of Physiochemical Properties and Bath Chemistry on Alumina Dissolution Rate in Cryolite Electrolyte. *The Journal of The Minerals, Metals & Materials Society* **2015**, *67* (5), 973-983.
12. Welch, B.; Kuschel, G., Crust and Alumina Powder Dissolution in Aluminum Smelting Electrolytes. *The Journal of The Minerals, Metals & Materials Society* **2007**, *59* (5), 50-54.
13. Perander, L.; Zujovic, Z.; Kemp, T.; Smith, M.; Metson, J., The nature and impacts of fines in smelter-grade alumina. *The Journal of The Minerals, Metals & Materials Society* **2010**, *61* (11), 33-39.
14. Perander, L.; Klet, C.; Wijayarathne, M.; Hyland, M.; Stroeder, M.; Metson, J., Impact of Calciner Technologies on Smelter Grade Alumina Microstructure and Properties. In *The 8th International Alumina Quality Workshop*, 2008.

15. Boom, E.; Cloutt, B. In *Hydrate Toughness Development and Application: Breakage Index*, The 11th Alumina Quality Workshop Conference, Gladstone, Queensland, Australia, Gladstone, Queensland, Australia, 2018; pp 99-106.
16. Zhang, J.; Ge, L.; Chen, Z.; Boom, E.; Zhu, Z., Cracking Behaviour and Mechanism of Gibbsite Crystallites during Calcination. *Crystal Research and Technology* **2018**, *54* (1), 1800201-1800208.
17. Zhang, J.; Ge, L.; Chen, Z.; Zhu, Z., Cracking behaviour and mechanism at grain boundary of gibbsite during calcination. *Ceramics International* **2020**, *46*, 12067-12072.
18. Zhou, W.; Xu, K.; Ma, G.; Chang, X., On the breakage function for constructing the fragment replacement modes. *Particuology* **2019**, *44*, 207-217.
19. Tyrrell, R.; De Souza, B.; Frawley, P., Particle Breakage: Limiting Conditions for Crystal–Crystallizer Collisions. *Crystal Growth & Design* **2018**, *18* (2), 617-622.
20. Perander, L. Evolution of Nano- and Microstructure during the Calcination of Bayer Gibbsite to Produce Alumina. The University of Auckland, 2010.
21. Leißner, T.; Hoang, D.; Rudolph, M.; Heinig, T.; Bachmann, K.; Gutzmer, J.; Schubert, H.; Peuker, U., A mineral liberation study of grain boundary fracture based on measurements of the surface exposure after milling. *International Journal of Mineral Processing* **2016**, *156*, 3-13.
22. Alex, T.; Kumar, R.; Roy, S.; Mehrotra, S., Mechanically induced reactivity of gibbsite: Part 1. Planetary milling. *Powder Technology* **2014**, *264*, 105-113.
23. Dodd, J.; Frances, C.; Guigon, P.; Thomas, A., Investigations into Fine Grinding. *KONA Powder and Particle Journal* **1995**, *13* (113-124).
24. Sang, J., Factors Affecting the Attrition Strength of Alumina Products. In *Light Metals 1987*, Zabreznik, R., Ed. 1987.
25. López, J.; Quintero, I., Evaluation of agglomeration stage conditions to control alumina and hydrate particle breakage. In *Light Metals*, 1991; pp 199-202.
26. Wind, S.; Jensen-Holm, C.; Raahauge, B., Development of Particle Breakdown and Alumina Strength During Calcination. In *Essential Readings in Light Metals: Volume 1 Alumina and Bauxite*, Donaldson, D.; Raahauge, B. E., Eds. Springer International Publishing: Cham, 2010; pp 757-764.

27. Klett, C.; Missalla, M.; Bligh, R., Improvement of Product Quality in Circulating Fluidized Bed Calcination. In *Light material 2010*, Johnson, J., Ed. 2010; pp 33-38.
28. Gan, B.; Madsen, I.; Hockridge, J., In situ X-ray diffraction of the transformation of gibbsite to α -alumina through calcination: effect of particle size and heating rate. *Journal of Applied Crystallography* **2009**, *42* (4), 697-705.
29. Malki, A.; Mekhalif, Z.; Detriche, S.; Fonder, G.; Boumaza, A.; Djelloul, A., Calcination products of gibbsite studied by X-ray diffraction, XPS and solid-state NMR. *Journal of Solid State Chemistry* **2014**, *215*, 8-15.

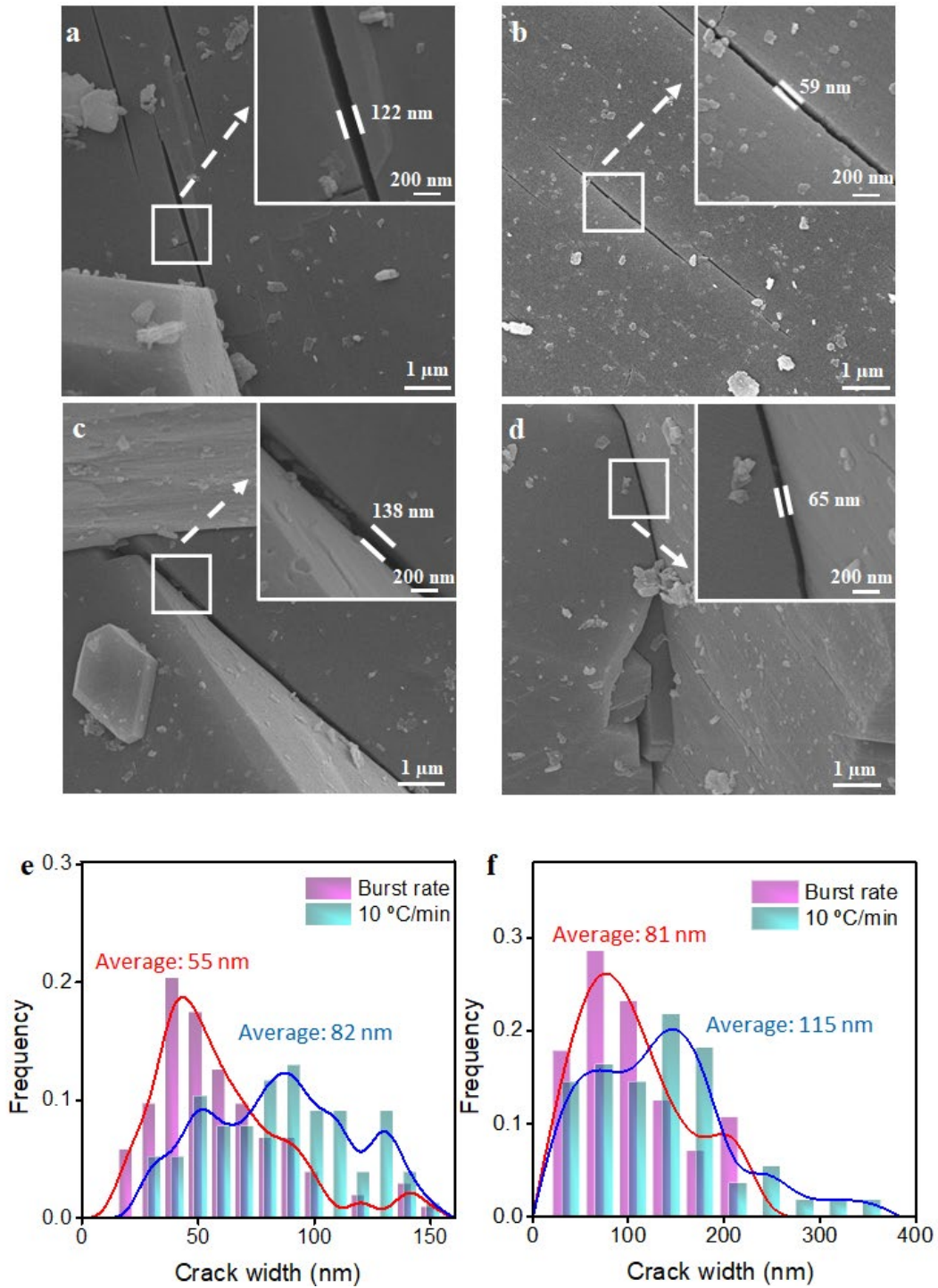


Figure 1 Typical SEM images of cracks in (a-b) crystallite in mosaic particles calcined at $10\text{ }^{\circ}\text{C}\cdot\text{min}^{-1}$ and at burst rate (c-d) grain boundary in mosaic particles calcined at $10\text{ }^{\circ}\text{C}\cdot\text{min}^{-1}$ and at burst rate, respectively. The width distribution of cracks within (e) crystallites and (f) grain boundaries in mosaic gibbsite particles calcined at $10\text{ }^{\circ}\text{C}\cdot\text{min}^{-1}$ and at burst rate. The calcination temperature is $400\text{ }^{\circ}\text{C}$.

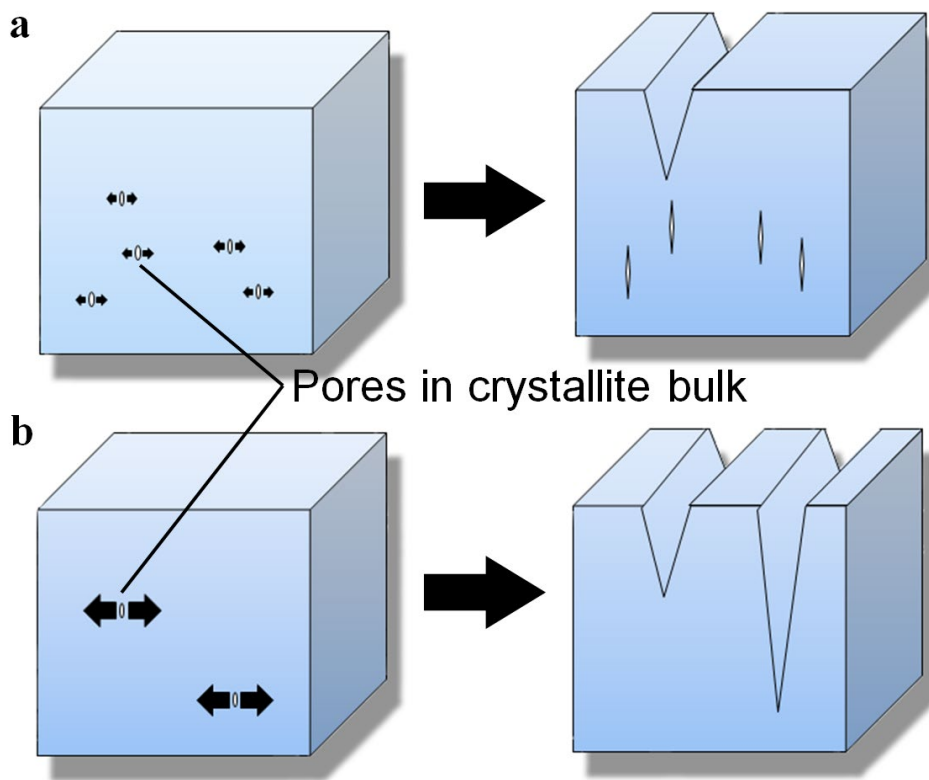


Figure 2 Sketch of crack generation in gibbsite crystallite during calcination with (a) higher ramping rate and (b) lower ramping rate

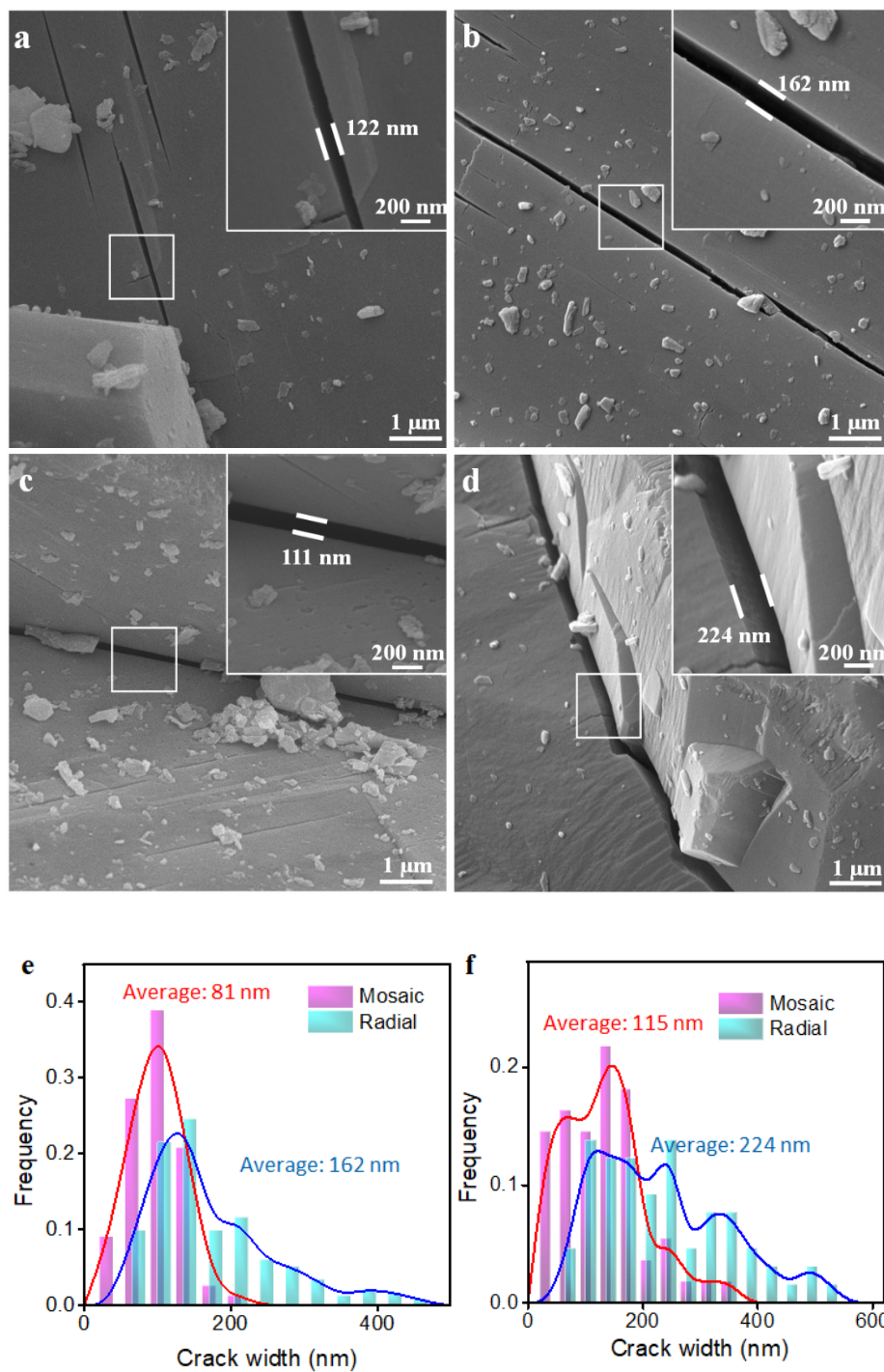


Figure 3 Typical SEM image of cracks on crystallite of (a) mosaic and (b) radial particles; grain boundaries of (c) mosaic and (d) radial particles calcined at 400 °C with 10 °C•min⁻¹. The width distribution of cracks within (e) crystallites and (f) grain boundaries in mosaic and radial particles calcined at 400 °C with 10 °C•min⁻¹.

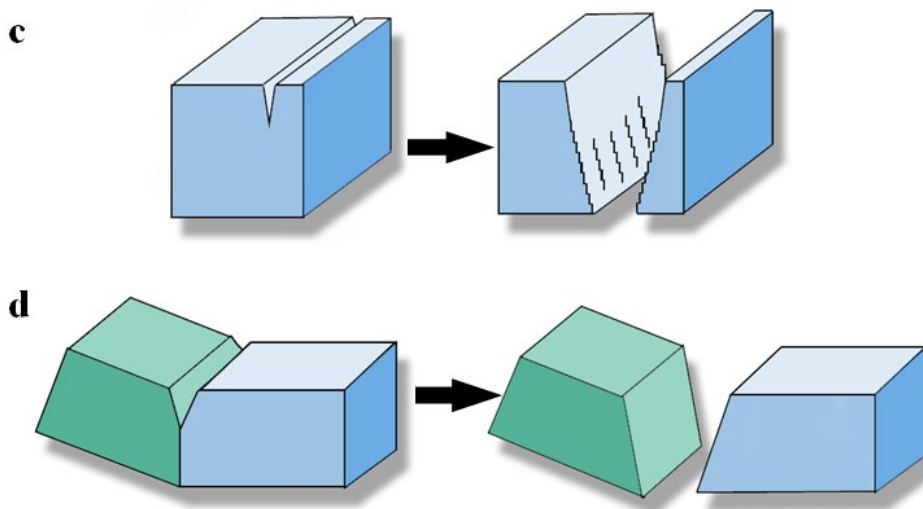
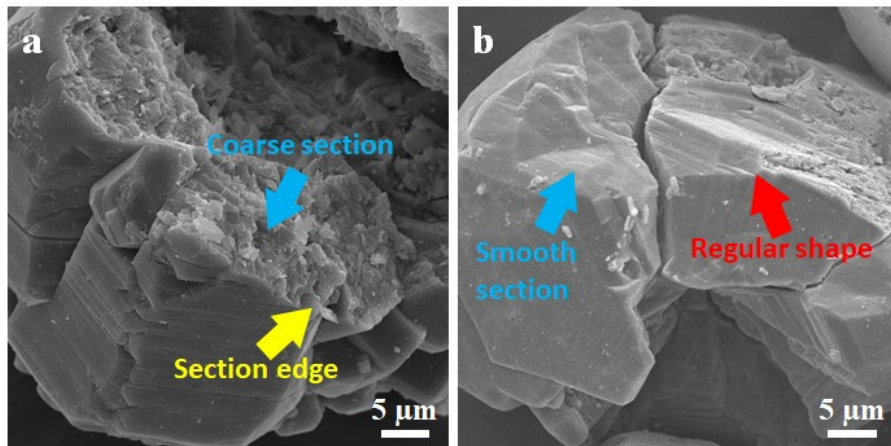


Figure 4 Typical SEM images of calcined gibbsite debris after SPI, (a) particle broken within crystallite (b) particle broken along the grain boundary. Scheme of calcined gibbsite breakage mechanism (c) within crystallite (d) along the grain boundary

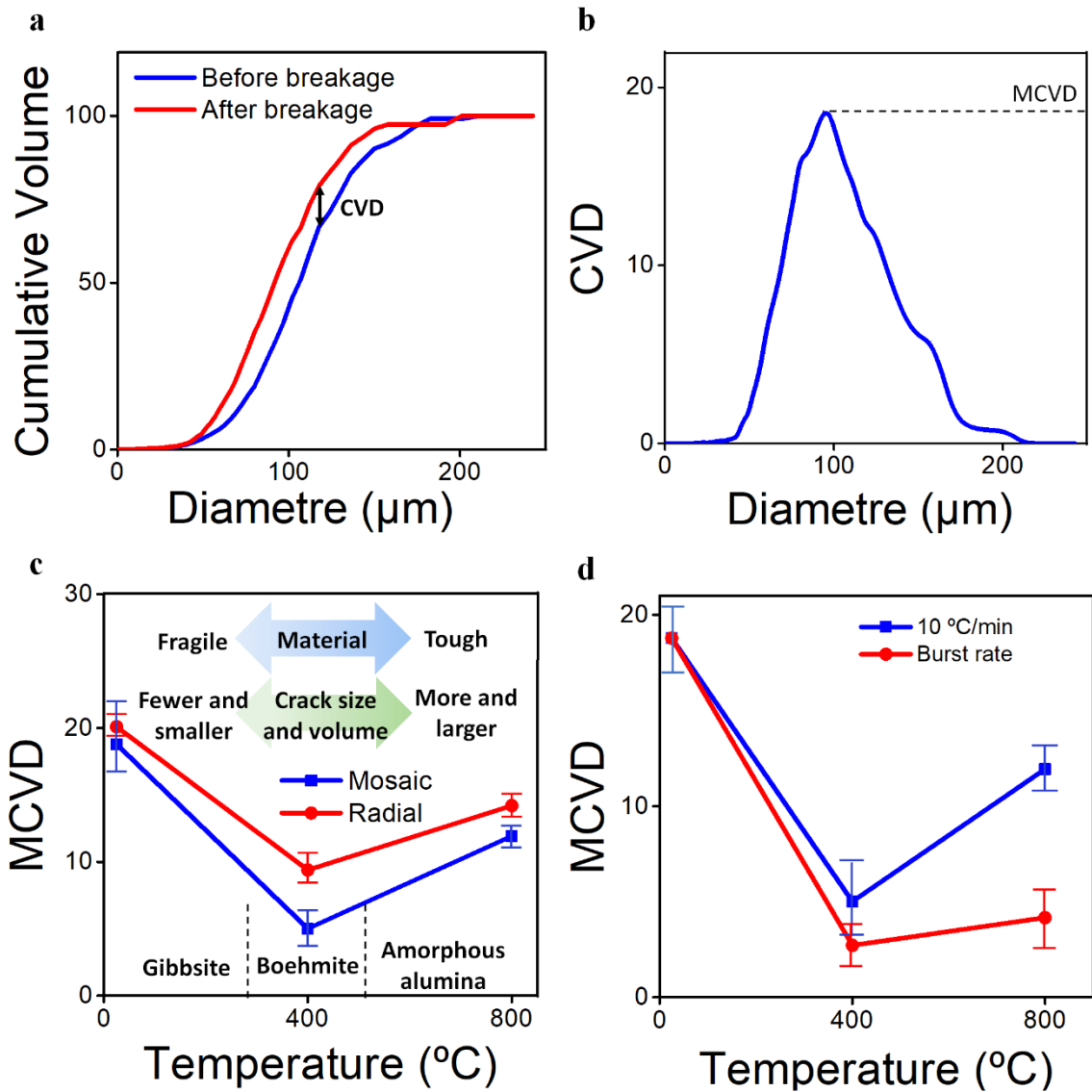


Figure 5 Cumulative volume distributions for gibbsite particles before and after breakage (b) Cumulative volume difference (CVD) distribution and the maximum cumulative volume difference. (c) MCVD of mosaic and radial gibbsite particles calcined at different temperatures. (d) MCVD of mosaic gibbsite calcined at different calcination ramping rates

Supporting information

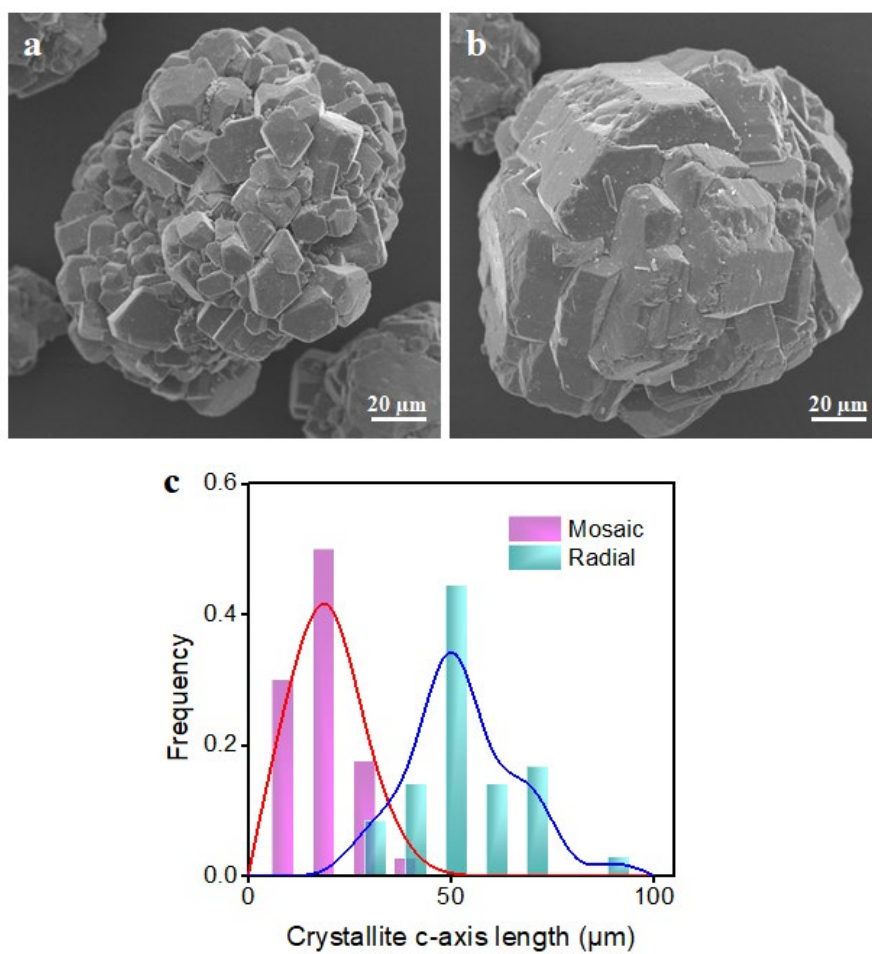


Figure S1 Typical SEM images of (a) mosaic and (b) radial gibbsite particles. (c) Crystallite c-axis length distribution of mosaic and radial gibbsite.

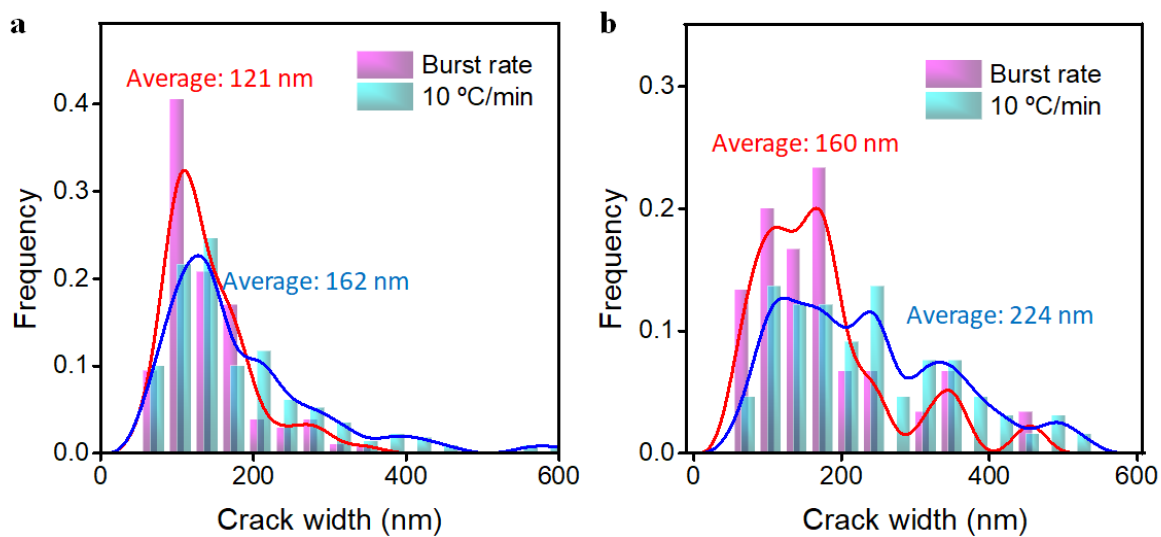


Figure S2 The width distribution of cracks within (a) crystallites and (b) grain boundaries in radial gibbsite particles calcined with $10\text{ }^{\circ}\text{C} \cdot \text{min}^{-1}$ and burst rate

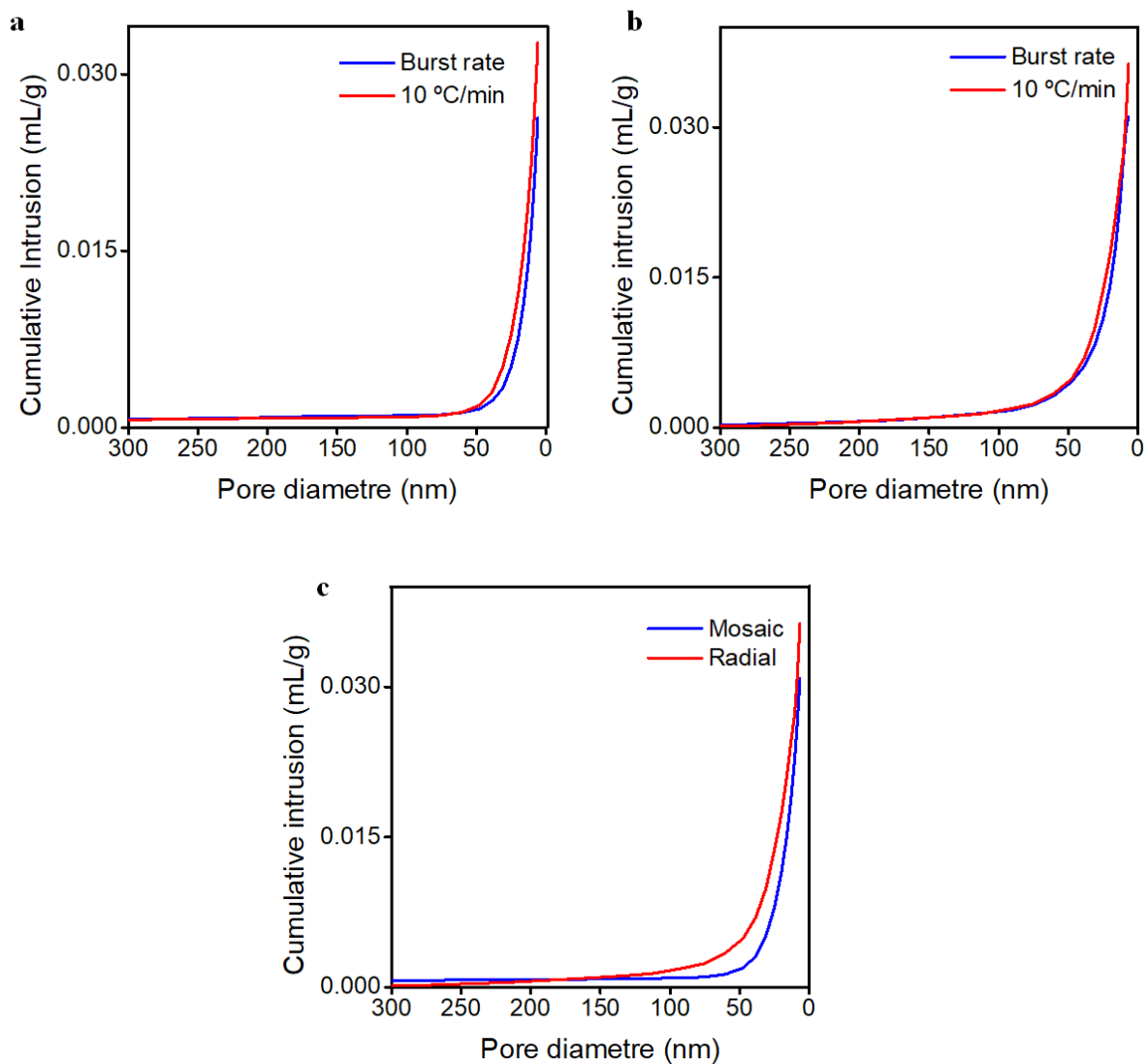


Figure S3 The cumulative intrusion of (a) mosaic gibbsite calcined at 400 °C with 10 °C • min⁻¹ and burst rate (b) radial gibbsite calcined at 400 °C with 10 °C • min⁻¹ and burst rate (c) mosaic and radial gibbsite calcined at 400 °C with 10 °C • min⁻¹.

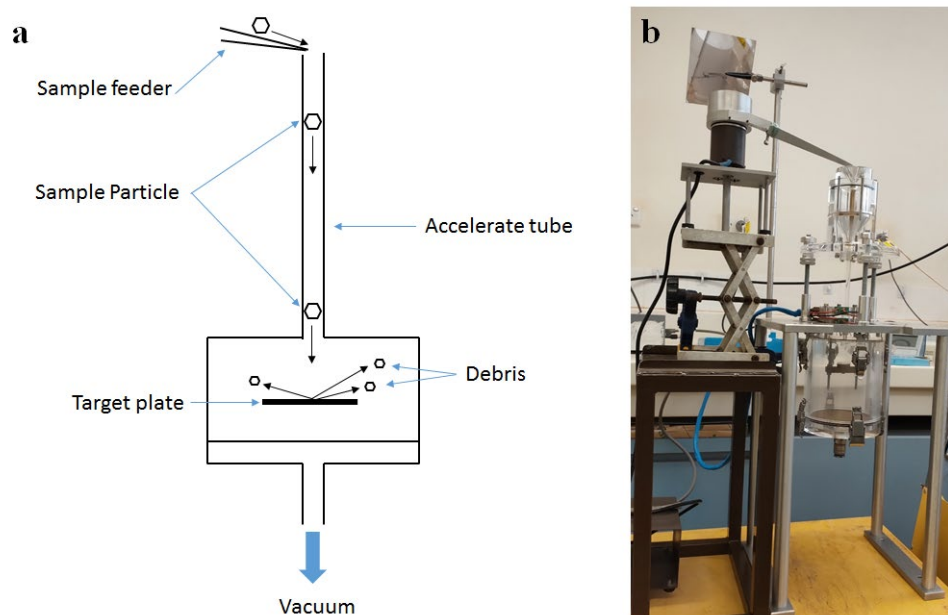


Figure S4 (a) Scheme and (b) picture of single-particle impact apparatus

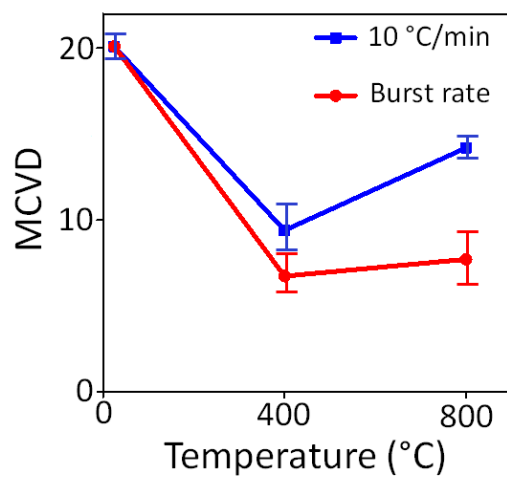


Figure S5 MCVD of radial gibbsite particles calcined at different ramping rates